



# Morphological Analyses of Polymer Electrolyte Fuel Cell Electrodes with Nano-Scale Computed Tomography Imaging

S. Litster<sup>1\*</sup>, W. K. Epting<sup>1</sup>, E. A. Wargo<sup>2†</sup>, S. R. Kalidindi<sup>2</sup>, E. C. Kumbur<sup>2</sup>

<sup>1</sup> Department of Mechanical Engineering, Carnegie Mellon University, Pittsburgh, PA 15213, USA

<sup>2</sup> Department of Mechanical Engineering and Mechanics, Drexel University, Philadelphia, PA 19104, USA

<sup>†</sup> Present address: George W. Woodruff School of Mechanical Engineering, Georgia Institute of Technology, Atlanta, GA, 30332

Received January 07, 2013; accepted June 25, 2013; published online ■■■

## Abstract

We report a three-dimensional (3D), pore-scale analysis of morphological and transport properties for a polymer electrolyte fuel cell (PEFC) catalyst layer. The 3D structure of the platinum/carbon/Nafion electrode was obtained using nano-scale resolution X-ray computed tomography (nano-CT). The 3D nano-CT data was analyzed according to several morphological characteristics, with particular focus on various effective pore diameters used in modeling gas diffusion in the Knudsen transition regime, which is prevalent in PEFC catalyst layers. The pore diameter metrics include those based on chord length distributions, inscribed spheres, and surface area. Those pore diameter statistics are evaluated against computational pore-scale diffusion simulations

with local gas diffusion coefficients determined from the local pore size according to the Bosanquet formulation. According to our comparison, simulations that use local pore diameters defined by inscribed spheres provide effective diffusion coefficients that are consistent with chord-length based estimations for an effective Knudsen length scale. By evaluating transport rates in regions of varying porosity within the nano-CT data, we identified a Bruggeman correction scaling factor for the effective diffusivity.

**Keywords:** Catalyst Layer, Computed Tomography, Fuel Cell, Knudsen Diffusion, Nano-CT, Transport

## 1 Introduction

Efficient energy conversion in porous electrodes depends on the combined efficacy of the electrochemical reaction kinetics, the electrode architecture, and the transport phenomena. This is particularly true for polymer electrolyte fuel cell (PEFC) electrodes, which are often referred to as catalyst layers. Due to the combination of the sluggish oxygen reduction reaction kinetics and the inherent oxygen and proton transport resistance introduced by state-of-the-art electrode materials, the effectiveness of the Pt utilization can be as low as 10% [1, 2]. In other words, the catalyst layer's current density is only 1/10th that if the transport rates were infinitely fast. There is great interest in reducing these transport resistances, since the electrode and the Pt raw material is the largest projected cost in high volume manufacturing of automotive PEFC stacks [3].

Typical PEFC electrodes consist of a network of carbon black aggregates bound by polymer electrolyte (e.g. Nafion) [4]. Dispersed Pt or Pt-alloy catalyst nanoparticles are supported by the carbon black particles. Electrochemical reactions occur at the triple phase boundaries where the proton, electron, and reactant pathways intersect at Pt surfaces. The electrodes have a packed agglomerate structure with small primary pores in the agglomerates and larger secondary pores between them [5]. The agglomerate size and pore size distribution depend on the slurry's solvent and preparation [4–7].

[\*] Corresponding author, [litster@andrew.cmu.edu](mailto:litster@andrew.cmu.edu)

### 1.1 Nano-Scale Imaging of PEFC Electrodes

Nano-scale 3D imaging of PEFC electrode structures is receiving increasing attention as research continues to identify that local transport resistances at the particle and agglomerate scales are responsible for large performance losses [8–11]. Thus, it is valuable to have direct quantification of the 3D electrode structure to evaluate different electrode formulations and to obtain morphological inputs for modeling. Two techniques have emerged in recent years for imaging the three-dimensional structure of electrodes: focused ion beam milling combined with scanning electron microscopy (FIB–SEM), and nano-scale X-ray computed tomography (nano-CT). Ziegler et al. [12] and Zils et al. [13] recently used FIB–SEM to image the structure of PEFC electrodes at high resolutions (10–30 nm voxel lengths). Although, FIB–SEM offers high spatial resolution, it is limited by the need for a vacuum environment and the destructive milling operation. For the micro-porous layer (MPL), which has a structure and scale very similar to catalyst layers, Wargo et al. [14] used FIB–SEM data to computationally evaluate the morphology and transport properties of the MPL. Similarly, there has been a substantial amount of work done using FIB–SEM and nano-CT to image the internal structure of solid oxide fuel cell materials for geometric input to transport simulations [15–19].

Recently, we demonstrated the use of 50 nm resolution (32.5 nm voxels) nano-CT to image PEFC electrodes [20]. Nano-CT benefits from allowing ambient and controlled environments and being non-destructive. Unfortunately, neither FIB–SEM nor nano-CT has yet been shown to separately distinguish the Pt, carbon, and Nafion constituent materials. However, our prior nano-CT imaging successfully provided the solid and pore phase size distributions, where the solid phase in the nano-CT data is comprised of the carbon, platinum, Nafion, and primary pores. In a previous publication [9], we used the computed solid phase's size distribution to examine the effect of an agglomerate size distribution on the current density predicted by the commonly used agglomerate model [11].

In addition to direct visualization, several research groups have computationally generated particle-scale and agglomerate-scale electrode structures, using these to evaluate transport properties and simulate coupled transport and electrochemical reaction [21, 22]. Often these reconstructions are informed by two-dimensional imaging of electrodes, usually by transmission electron microscopy (TEM). There are several routes to generating the structure. Muhkerjee and Wang [23] used the two-point correlation statistics from 2D TEM images to generate the 3D agglomerate structure. Kim and Pitsch [21] used an annealing algorithm to generate a representative particle agglomerate structure based on two-point correlation statistics that was verified against mercury intrusion porosimetry data. Lange et al. [22] randomly placed spheres within a computational volume using rules regarding the placement of new seed particles and particle overlap. Once generated,

those computational reconstructions can be used in transport simulations for identifying effective transport properties for representative elementary volumes [21] as well as to perform particle-scale or agglomerate simulations of the coupled transport and reactions during operation [22, 23]. Amongst the PEFC work above, there is still a lack of gas diffusion simulation analysis on directly measured three-dimensional pore geometry. This motivates the present study since a true three-dimensional geometry input is necessary to properly capture diffusivity anisotropy and other properties that require an accurate portrayal of the three-dimensional structure.

In this paper, we report on the use of nano-scale resolution X-ray CT and computational simulations to obtain morphological and transport properties for a PEFC catalyst layer. Our analysis includes an assessment of several morphological pore size characteristics based on chord lengths, inscribed spheres, and surface area. We take particular interest in characteristics related to Knudsen gas diffusion. These characteristics are evaluated against those obtained from pore-scale simulations of gas transport in the 3D reconstructed catalyst layer.

## 2 Methods

### 2.1 Electrode Preparation and Nano-CT

The details of the electrode preparation and the nano-CT imaging are discussed in our previous publication [20]; herein we briefly review that process. The electrode was prepared from a mixture of 20% Pt/C catalyst where the catalyst support was Vulcan XC72R (Electrochem, Inc., Woburn, MA) and 5 wt.% Nafion solution (DE-521, Ion Power, Inc., New Castle, DE), where proportions were specified for a Nafion loading of 35 wt.%. The ionomer to carbon ratio (I/C) was 0.65. The mixture was ultrasonicated (dip-type) for 10 min and then stirred overnight on a magnetic stirrer. The ink was then hand-painted onto a 50  $\mu\text{m}$  thick Kapton HN film (Dupont, Wilmington, DE). Successive painting and then drying in an oven at 110  $^{\circ}\text{C}$  was done until the loading reached 0.9 mg Pt  $\text{cm}^{-2}$ , resulting in an approximately 70  $\mu\text{m}$  thick electrode. In the nano-CT imaging [20], there was no discernible effect of the layer-by-layer or the Kapton film interface on the electrode structure. We prepared the electrode with this exaggerated thickness to increase the material volume and decrease the surface to volume ratio for mercury intrusion porosimetry measurements.

A nano-CT (UltraXRM L200, Xradia, Inc., Pleasanton, CA) was used to image the three-dimensional electrode structure with an 8 keV X-ray beam focused by a capillary condenser and Fresnel zone plate objective [24]. For imaging in the nano-CT, the electrode/Kapton film was cut to have a triangular point that would fit into the field of view and then inserted into a clip-type sample holder. The lower portion of the triangular section (below the field of view) was folded over the vertical axis to increase stability and reduce sample drift during the scan. The Zernike phase contrast imaging

mode was used to enhance the interfaces of the low Z electrode materials. The resulting radiograph series were reconstructed into a three-dimensional image with 32.5 nm cubic voxels. Figure 1 shows a three-dimensional reconstruction of the electrode solid phase. In our prior work, we verified the CT data against mercury intrusion porosimetry and TEM micrographs of the same catalyst layer [20].

## 2.2 Structural Morphology

Several morphological characteristics are purely structural and do not require imposing a transport mechanism for the analysis. Herein, we report structural morphology characterizations that include volumetric surface area, chord-length distributions, and shortest-path tortuosity. Previously, we characterized the morphology of the electrode by porosity and size distributions based on inscribed spheres [20].

Our internal surface area computation uses MATLAB's "isosurface" function (MATLAB version R2010b, The MathWorks Inc., Natick, MA) to compute a triangulated mesh which encloses the void (pore) space within the reconstruction. The area of this mesh is determined in pixels, which is multiplied twice by the voxel size of 32.5 nm to get the actual internal surface area, and then divided by the total volume of the reconstruction to obtain the internal surface area per unit volume.

Chord length distributions are used here to capture the size distribution of a given phase (i.e. pore, solid) within the 3D electrode reconstruction. A chord is defined as a line of specific orientation which connects two phase boundaries within a material structure while lying completely within a single material phase [25]. The procedure finds the length of every chord within the 3D voxelated structure at the given orientation and within the phase of interest, resulting in a chord length distribution for that phase-orientation combination [25]. Distributions may be obtained at several orientations to increase resolution or identify anisotropic characteristics. For simplicity, in this study, only the three primary orthogonal orientations of the volume are considered.

The shortest-path tortuosity  $\sqrt{\tau_{SP}}$  is analyzed using a shortest path search method that can identify all the tortuous paths and compute the spatial distribution of tortuosity for a

given microstructure [14, 25]. It is important to note that the shortest-path tortuosity is independent of transport, and it is distinct from the tortuosity obtained from diffusive transport analysis. The method here uses Dijkstra's algorithm to search for the shortest path through the pore space from a voxel on the entry surface to the exit surface [14, 25]. The length of the tortuous path is then divided by the shortest distance between the entry and exit surfaces (i.e. the thickness of the volume) to determine the tortuosity value for that specific path. Accordingly, a path may be identified from every pore voxel on the entry surface, resulting in a distribution of tortuosity for the 3D material structure. With this approach, a value can be computed for every surface pixel, yielding a shortest-path tortuosity distribution.

## 2.3 Morphological Transport Properties

In addition to the structural characteristics described above, we have also characterized the transport-dependent morphological properties. The properties reported herein include the tortuosity, formation factor, and diffusion coefficient anisotropy for the pore phase and solid phase volumes of the nano-CT data. To obtain these characteristics, we performed finite element method simulations on the pore-scale nano-CT data, where diffusion and conduction are approximated by the Laplace equation:

$$\nabla(D\nabla c) = 0 \tag{1}$$

where  $D$  is the transport coefficient (i.e. the diffusion coefficient or conductivity) and  $c$  is the concentration or potential. The concentration is arbitrarily specified as 0 and 1 at two opposing faces of the cubic domain, and the flux is set to zero at all adjacent faces.

In our approach, we simulate transport in the porous material by assigning local diffusivities. We locally specify the diffusion coefficient in the pores as a function of pore diameter  $d_{pore}$  because the electrode's pore diameters are close to the mean free path of the gas molecules, and thus it is important to account for the diameter-dependent Knudsen diffusion. We neglect diffusion coefficient variations in the solid phase.

A simple form of the Bosanquet formula is used to determine the local Knudsen transition regime gas diffusion coefficient ( $D_B$ ) as the series resistance of molecular and Knudsen diffusion:

$$\frac{1}{D_B(d_{pore})} = \frac{1}{D_{Kn}(d_{pore})} + \frac{1}{D_m} \tag{2}$$

where  $D_m$  and  $D_{Kn}$  are the molecular and Knudsen diffusion coefficients, respectively. The Knudsen diffusion coefficient is calculated as a function of the pore diameter according to the formula:

$$D_{Kn}(d_{pore}) = \frac{d_{pore}}{3} \sqrt{\frac{8RT}{\pi M}} \tag{3}$$

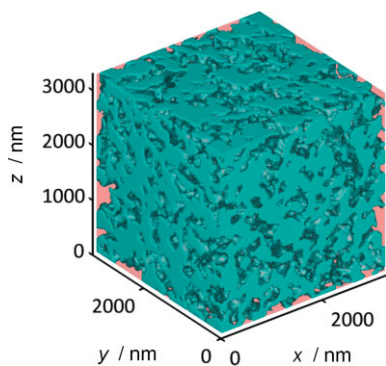


Fig. 1 Reconstruction of electrode solid phase from nano-CT imaging.

The temperature dependence for molecular diffusion was included by the following scaling:

$$D_m = D_m^{\text{ref}} \left( \frac{T}{T_{\text{ref}}} \right)^{1.75} \quad (4)$$

For the oxygen diffusion simulations herein, we use a reference molecular oxygen diffusivity of  $D_m = 3.07 \times 10^{-5} \text{ m}^2 \text{ s}^{-1}$  at 373 K [26]. By using the published value for oxygen diffusivity, we do not explicitly consider the oxygen's mean free path or diameter. In simulations of transport properties for the solid phase, the local solid diffusion coefficient is set to a spatially-uniform value of 1.

## 2.4 Effective Transport Properties

Once simulations are completed, the transport properties are computed from the resulting flux integrals at the boundaries. The effective diffusion coefficient,  $D_{\text{eff}}$ , is computed from the area flux integral,  $J$ , at the outlet or inlet boundary for a specified concentration difference,  $\Delta c$ , from inlet to outlet:

$$D_{\text{eff}} = \frac{J L}{A \Delta c} \quad (5)$$

where  $A$  is the boundary area, and  $L$  is the distance between the inlet and outlet boundaries. The effective diffusivity can also be expressed as a function of the pore volume fraction (porosity,  $\varepsilon$ ) and the tortuosity factor,  $\tau$ :

$$D_{\text{eff}} = \frac{\varepsilon \bar{D}}{\tau} \quad (6)$$

The tortuosity factor  $\tau$  is the square of the tortuosity, which is defined as the ratio of the mass-flow averaged flow pathline lengths to the straight, point-to-point length:

$$\tau = \left( \frac{\langle \text{pathline lengths} \rangle}{\text{point to point length}} \right)^2 \quad (7)$$

The power of two in the expression above arises from the combined effects of the increased length of the pore and the reduced interstitial gradients due to the tortuous paths [27]. Knowing the effective diffusivity from the simulation result and the volume-averaged diffusion coefficient in the pore phase,  $\bar{D}$ , we calculate the tortuosity factor:

$$\tau = \frac{\varepsilon \bar{D}}{D_{\text{eff}}} \quad (8)$$

where  $\bar{D}$  is the volume-averaged diffusion coefficient in the pores:

$$\bar{D} = \frac{1}{V_{\text{pore}}} \int_{V_{\text{pore}}} D dV \quad (9)$$

In some instances, it is preferable to correct bulk diffusion coefficients with a single correction parameter rather than the combination of the volume fraction and tortuosity. In these instances, the formation factor is reported, which is classically considered the ratio of the bulk resistance of a conducting media to that of the conducting media when saturating a non-conductive porous material.

$$K_f = \frac{D_{\text{eff}}}{\bar{D}} \quad (10)$$

In light of Eq. (6), one could consider the formation factor,  $K_f$ , as one lumped parameter that replaces the porosity and tortuosity:

$$K_f = \frac{\varepsilon}{\tau} \quad (11)$$

The work of De La Rue and Tobias [28] and many subsequent works have demonstrated the adequacy of a Bruggeman correction, which is a simple power law scaling for the formation factor as a function of the porosity when sufficiently far from the percolation limit:

$$D_{\text{eff}} = \varepsilon^a \bar{D} \quad (12)$$

De La Rue and Tobias [28] showed that the value of  $a$  is very close to 1.5 when the volume fraction of a dispersed insulating phase is sufficiently low. This value is commonly assumed in fuel cell models [29].

## 2.5 Numerical Method

The transport simulations were performed using COMSOL 3.5a finite element multiphysics software (COMSOL, Inc., Burlington, MA). The COMSOL operation was scripted using MATLAB to enable automated generation of geometry and parametric simulations directly from X-ray CT planar slice images. Rather than generating a surface for the pore | solid interface and generating a body-fitted mesh, in our approach we mesh the entire domain and locally assign the diffusion coefficient. For gas diffusion simulations, a diffusion coefficient of zero is specified wherever the location is in the solid phase. In the transition regime simulations, the local diffusion coefficients are specified based on the local pore diameter, which was evaluated using a morphological opening algorithm that combines erosion and dilation operations with a spherical kernel. The local pore sizes for each voxel are written to a lookup file by MATLAB that is later read by the COMSOL solver to locally specify the diffusion coefficient. In this work, we used the Paradiso solver with four levels of tetrahedral mesh refinement. After the four levels of refinement, the solver was re-run with the most refined mesh with higher convergence tolerance criteria. The morphological transport properties are automatically post-processed by MATLAB for efficient analysis of large sample sets.

## 3 Results and Discussion

### 3.1 Structural Morphology

#### 3.1.1 Chord Length Distribution

Average chord length distributions based on chord orientations in the three primary orthogonal directions ( $x$ ,  $y$ , and  $z$ ) were determined for both the solid and pore phases of the electrode reconstruction. The solid phase results shown in Figure 2a indicate that the solid phase agglomerates of the

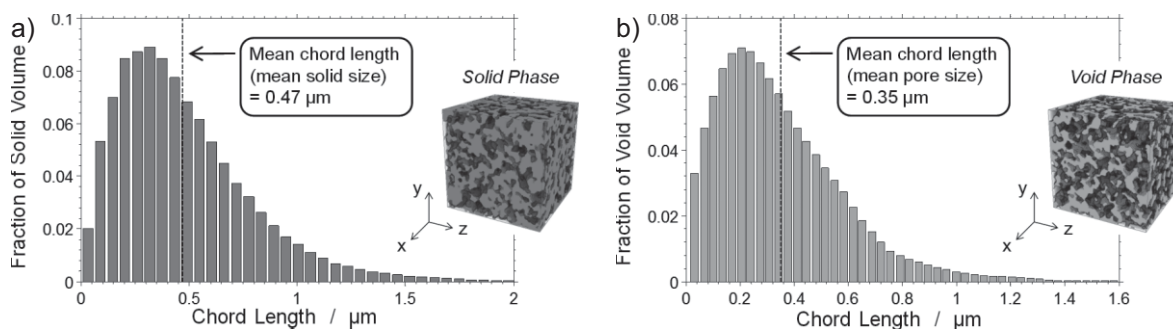


Fig. 2 Chord length distributions for (a) the solid phase and (b) the void phase of the electrode reconstruction.

catalyst layer structure are generally below 1  $\mu\text{m}$  in size, with an average chord length of 0.47  $\mu\text{m}$  and a peak around 0.3  $\mu\text{m}$ . In contrast, the volume averaged solid phase diameter based on inscribed spheres is 190 nm [20]. Similarly, Figure 2b shows that the chord lengths within the pores of the electrode are primarily below 0.7  $\mu\text{m}$ , with an average chord length of 0.35  $\mu\text{m}$  and a peak near 0.2  $\mu\text{m}$ . For comparison, the voxel-averaged mean pore diameter based on inscribed spheres is 165 nm [20]. For air at 330 K and 1 atm of pressure, this pore diameter yields a Knudsen number ( $Kn$ ) of 0.45, which is well within the bounds of the Knudsen transition regime.

Within the literature, there is a wide array of proposed measures of representative pore diameter, particularly in relation to the appropriate length scale for Knudsen diffusion. Table 1 lists several effective pore diameters, including those based on inscribed spheres, volumetric surface area, and the chord length distribution. The volumetric surface area  $A_s$  can be converted to an effective diameter using the porosity,  $\varepsilon$ , and the equation  $d = 4\varepsilon/A_s$  [30], which is geometrically consistent with the assumption of cylindrical pores. The pore diameter of our reconstruction based on surface area is 216 nm, which is 30% larger than that based on the inscribed spheres due to surface irregularities. In addition, the mean chord length  $\langle l \rangle$  of 351 nm is 63% larger than the surface area estimate due to the long chord lengths in the axial direction of the pores.

For Knudsen diffusion, B.V. Derjaguin used an analytical analysis, later presented by Henrion [30], to derive a mean path length between wall collisions based on the mean chord length  $\langle l \rangle$  and the mean squared chord length  $\langle l^2 \rangle$

$$d = \left( \frac{\langle l^2 \rangle}{2\langle l \rangle^2} - \beta \right) \langle l \rangle \quad (13)$$

Table 1 Effective pore diameters,  $d$ , and related parameters based on pore geometry in a  $3.2 \mu\text{m} \times 3.2 \mu\text{m} \times 3.2 \mu\text{m}$  sample volume.

Parameter	Value
$d = 2(d_{\text{sphere}})$	165 nm
$A_s$	$7.76 \mu\text{m}^2 \mu\text{m}^{-3}$
$d = 4\varepsilon/A_s$	216 nm
$\langle l \rangle$	351 nm
$\langle l^2 \rangle$	$179,000 \text{ nm}^2$
$d = \langle l^2 \rangle / 2\langle l \rangle$	255 nm
$d = \langle l \rangle (\langle l^2 \rangle / 2\langle l \rangle^2 - \beta)$ , $\beta=4/13$	147 nm

where  $\beta$  corrects for the nature of the surface reflection (e.g. elastic *vs.* inelastic collisions) and can be derived using the cosine of the angle between particle trajectories for wall collisions. For specular, elastic reflections,  $\beta = 0$ , and  $d = \langle l^2 \rangle / 2\langle l \rangle$ . However,  $\beta \approx 4/13$  is often assumed to account for inelastic collisions for Knudsen diffusion when the collision is idealized as a serial adsorption and desorption event. It was proposed that direction of the desorbed molecule is uncorrelated with its direction during impact and further that the evaporated molecule is primarily emitted in a direction normal to the pore surface [30]. The papers by Henrion [30], Zalc et al. [31], and Berson et al. [32] are highly recommended for further review of these scalings and their analysis.

The first term in the brackets of Eq. (13) is 1 for an exponential chord length distribution and 0.67 for an infinitely long cylinder. The value of this term for the reconstructed electrode is 0.73. This similarity to the ideal cylinder value also supports the notion of approximately cylindrical pore geometry in addition to the earlier agreement for a surface area approximation for cylinders. Here, we adopt the  $\beta=4/13$  value for inelastic collisions under the assumptions that gas molecules will be primarily colliding with a Nafion polymer electrolyte film covering the catalyst particles, or with water present either within the Nafion polymer or existing as an additional adsorbed film. In Henrion's analysis of various collision models, the present  $\beta$ -value of 4/13 yields the lowest Knudsen diffusion coefficient estimates of those evaluated. As listed in Table 1, this  $\beta$  yields a representative pore diameter of 147 nm, which is similar to the value obtained for inscribed spheres.

### 3.1.2 Shortest-Path Tortuosity

Figure 3 presents the tortuous shortest path lengths computed through the electrode reconstruction in the  $y$ -direction and their corresponding distribution. It is important to note that these tortuosities are distinct from the conventional tortuosity factor used in porous media transport analysis. The shortest-path tortuosities are a measure of the shortest possible path from a point on the entry surface to any point on the exit surface. Thus, they do not account for the reduced cross-sectional area and restricted flow in smaller pores. Instead, these computed paths represent possible connected pathways for transport through the tortuous pore geometry, while the

actual paths will depend on the type of transport. The shortest-path tortuosity can be considered as a lower bound of the tortuosity, and may be useful for comparing different microstructures within a given class of materials. The shortest-path tortuosity distribution indicates that the electrode structure contains a fairly broad range of shortest path lengths. This distribution is based on data from 3,757 paths (entry points), yielding values ranging from 1.11 to 1.54 and a mean value of 1.30. In addition, the other orthogonal directions were also analyzed, giving mean shortest-path tortuosities of 1.24 ( $x$ -direction) and 1.32 ( $z$ -direction), indicating the existence of minor anisotropy.

## 3.2 Pore Phase Diffusion

In the previous sections, we presented the morphological characteristics that can be evaluated without invoking a transport mechanism; they were purely geometrical. In the following section, we present analysis of the morphological properties that depend on a particular transport mechanism or transport regime. In these analyses, we use pore-scale finite element simulations.

### 3.2.1 Adaptive Meshing and Grid Convergence

A mesh convergence study was performed to identify the number of adaptive meshing iterations required to obtain acceptable levels of conservation error and solution convergence. The study was performed on a  $1.265 \mu\text{m} \times 1.265 \mu\text{m} \times 1.265 \mu\text{m}$  volume within the nano-CT data. In this convergence study, we applied a uniform diffusion coefficient of 1 in the pores because it more heavily weights the impact of the smaller pores compared to using a Knudsen corrected diffusion coefficient that reduces the flux in smaller pores due to the reduced diffusivity. Figure 4 presents the results of the grid convergence study for both uniform element size meshes and four levels of mesh adaptation. The insets of Figure 4 show the porous regions of the sample volume and the corresponding increased mesh density in those locations with adaptive meshing. The smallest elements are concentrated at the pore/solid interfaces. The data markers indicate the average of the integrated fluxes across the

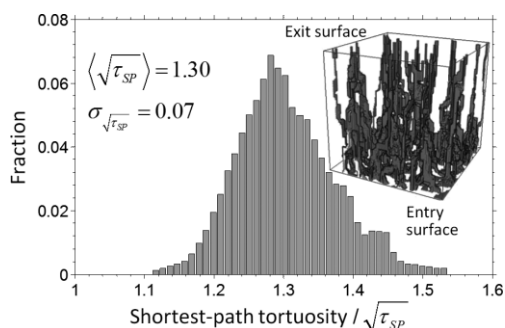


Fig. 3 Shortest-path tortuosity distribution for 3,757 paths originating from voxels on the entry surface. The inset shows a surface rendering of the computed pathways from the entry surface to the exit surface.

inlet and outlet faces, while the error bars indicates the difference between these two values of the integrated flux. The plots show that the grid converges with approximately  $10^6$  elements with both uniform and adaptive meshes. However, the conservation error is notably reduced with the adaptive meshing *versus* uniform meshing due to the smaller element sizes within the porous regions; at the highest level of refinement, the conservation error is  $<1\%$ .

### 3.2.2 Gas Diffusion Simulations

Transition regime gas diffusion simulations, as well as simulations using a hypothetical case of uniform molecular diffusivity, were performed on one large sample ( $2.53^3 \mu\text{m}^3$ ) and eight ( $1.265^3 \mu\text{m}^3$ ) sub-samples. The sub-sample results are used to evaluate spatial heterogeneity in the structure in the next section. Figure 5a shows the diffusion coefficient distribution on the surface of the large  $2.53^3 \mu\text{m}^3$  sample domain as well as the segmentation of the large sample into eight sub-samples. The transport simulations were separately performed in the three orthogonal directions ( $x, y, z$ ) to evaluate anisotropy.

Figure 5b presents a visualization of the gas diffusion. In those images, the pore wall is shaded by local concentration in the pore. The pore wall geometry is imaged by an interpolated isosurface at a diffusion coefficient value between zero (for the solid) and the lowest estimated value from the Bosanquet formulation. Streamlines are shown to indicate the tortuous paths through the structure and they are shaded by the local diffusion coefficient. The inset with the transparent walls shows the significantly more tortuous pathways in comparison to the shortest path images in Figure 3. This difference arises from the high diffusion resistance of the smaller diameter pores. This higher resistance forces some of the gas to take more tortuous paths through larger, less resistive pores.

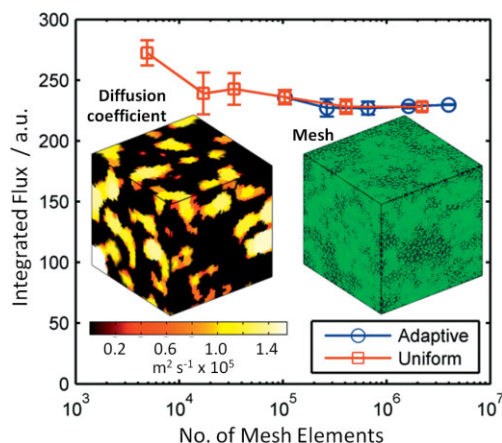


Fig. 4 Grid convergence results with uniform element size and adaptive meshing. The data points are the mean values between the inlet and outlet boundaries and the height of the error bars are the differences between the inlet and outlet boundaries. The insets show the pore diameter dependent diffusion coefficient from the Bosanquet formula (left) and the corresponding mesh from adaptive meshing (right).

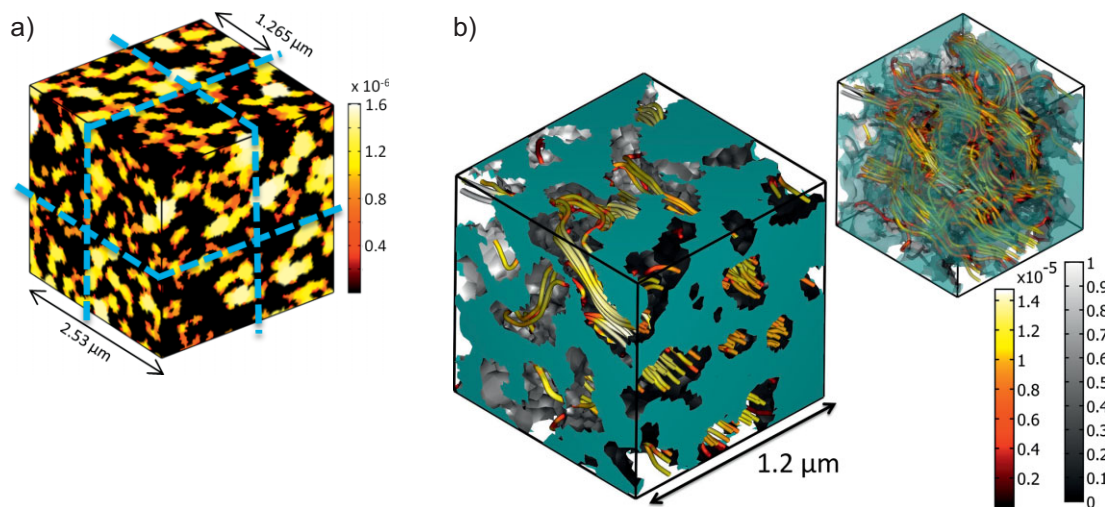


Fig. 5 (a) Knudsen transition regime diffusion coefficient for the large  $2.53 \mu\text{m} \times 2.53 \mu\text{m} \times 2.53 \mu\text{m}$  sample volume. The division of the volume into eight sub-samples is shown by dashed lines. (b) Results of an  $\text{O}_2$  diffusion simulation using the Bosanquet formula for the diffusion coefficient in one of the eight sub-samples. Gray-scale shading on pore walls shows concentration (based on arbitrary boundary conditions of 0 and 1). Streamlines for gas diffusion are colored by the local diffusion coefficient. The streamlines indicate tortuous gas pathways. The smaller inset shows the same instance, but with transparent pore walls to show the internal tortuous pathways.

### 3.2.3 Effect of Knudsen Diffusion and Temperature

Figure 6 shows the effective diffusivities of the eight sub-samples for the three orthogonal directions as a function of the sub-sample porosity. The plots include the effective diffusivity for the transition regime according to the Bosanquet formula at temperatures of 330 and 360 K. For reference, we also plot the effective diffusivity for molecular diffusion only (i.e. if Knudsen diffusion is neglected). The comparison at 330 K shows that the inclusion of Knudsen effects reduces the effective diffusivity by roughly a factor of 1/3 compared to values without Knudsen effects. In addition, the transition regime diffusivity is significantly more sensitive to porosity. The percent increase in the effective diffusion coefficient from the lowest porosity to the highest porosity was 41% for molecular diffusion, whereas for the transition regime it was 89%. This difference arises because of the relationship between the porosity and the pore sizes (lower porosity entails smaller pores) in concert with the Knudsen diffusion dependence on pore size.

In addition to temperature, simply changing the local pore diffusivity values, it can also potentially change the flow path lines. This is because increases in temperature yield increases in the Knudsen number, which in turn amplify the diffusion resistance in the smaller pores and redirects the diffusion through the larger pores. Thus, increases in temperature can decrease the formation factor by increases of the tortuosity factor. In this work, the increase of temperature from 330 to 360 K only decreased the formation factor by a negligible 0.3%, which indicates that the morphological properties reported here are effectively independent of temperature within a reasonable range of fuel cell operating temperatures.

### 3.2.4 Comparison with Experimental Data

Figure 6 also includes two experimental data points from the work by Yu and Carter [33] for their I/C values of 0.5 and 1.0. We plotted their values for a relative humidity of 50% since it is consistent with our imaging condition, and below that relative humidity their diffusion coefficient values are independent of relative humidity. Since the Yu and Carter data was obtained at 353 K, it can be compared with our 360 K results as illustrated by the small change in our diffusion coefficient values between 330 and 360 K. Although, they did not measure the diffusion coefficient of an electrode with the same ionomer to carbon ratio (I/C) as ours, a linear interpolation between their 0.5 and 1.0 I/C diffusivities gives a diffusivity of  $1.8 \times 10^{-6} \text{ m}^2 \text{ s}^{-1}$ , which compares well with our isotropic mean effective diffusivity of  $1.80 \times 10^{-6} \text{ m}^2 \text{ s}^{-1}$ . This

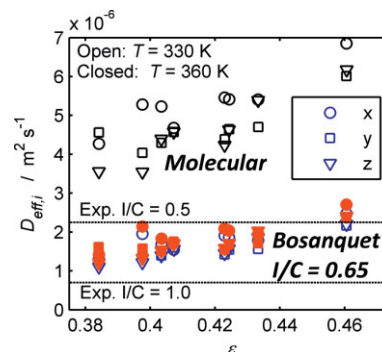


Fig. 6 Effective diffusivities for molecular diffusion and Knudsen transition regime diffusion according to the Bosanquet formulation in the three orthogonal directions. The transition regime diffusivity is shown for temperatures of 330 and 360 K. The molecular diffusion plot is for 330 K. The dotted horizontal lines are the diffusion coefficients measured by Yu and Carter [33] for catalyst layers with I/C ratios of 0.5 and 1.0 at 50% relative humidity and a temperature of 353 K. The simulation results are for a catalyst layer having an I/C ratio of 0.65.

exact agreement is fortuitous and should not be considered to show an exact prediction. Rather, it shows that simulation captures well the diffusion resistance magnitude. In addition, Figure 6 shows that the simulated effective diffusivities in different sub-samples and directions are well-bounded by the two experimental measurements. No fitting or model tuning was done to achieve this agreement.

### 3.2.5 Formation, Tortuosity, and Bruggeman Factors

Figure 7 presents plots of the formation factor for the eight sub-samples in the three orthogonal directions. The values for the large sample are also plotted. The formation factor values, on the order of 0.1, illustrate the nearly order of magnitude decrease in the diffusivity due purely to the pore morphology. The inset of Figure 7 plots the corresponding values of tortuosity that range between nearly 2 and 4, with large scatter at the lower porosities. However, there is a clear trend of decreasing tortuosity with greater porosity.

Using the formation factor values, we also plot lines for Bruggemann correction factor fits with a values for each direction as well as for an isotropic mean (values listed in Table 2). As noted earlier, transport in the Knudsen transition regime is more sensitive to the porosity. For example, the

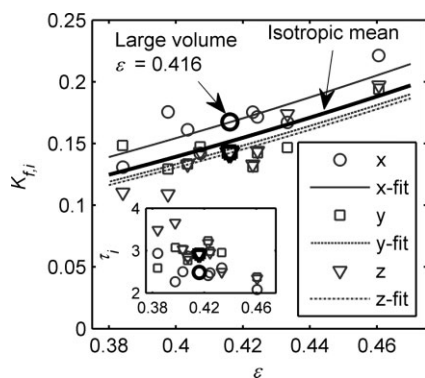


Fig. 7 Formation factor for the Knudsen transition regime in the pores at a temperature of 330 K. Data points are shown for the large  $2.53 \mu\text{m} \times 2.53 \mu\text{m} \times 2.53 \mu\text{m}$  sample volume (large, thick symbols) as well as for the eight equally sized sub-samples, versus their respective porosity, for the three orthogonal directions. Bruggeman power law fits for the porosity scaling are shown for each direction and for an isotropic average (thick line). The inset shows the corresponding tortuosity factors for the large volume and the eight smaller sub-samples.

Bruggemann factor for the isotropic mean effective diffusivity was 2.04 for uniform molecular diffusivity (no Knudsen effects) versus 2.15 when considering the Knudsen transition regime. In either case, these values are much higher than the commonly used value of 1.5, which apparently under predicts mass transport resistances in PEFC catalyst layers.

Care must be used in applying the Bruggemann factors reported here. First, the porosity reported here is that for pores resolved by the 32.5 nm nano-CT voxels with the true resolution somewhere between 50 and 80 nm. Thus, we are reporting the volume fraction of the larger, secondary pores, which does not include the smaller primary pores. In other words, the true porosity could be up to 10–15% higher. Fortunately, fuel cell electrode models often incorporate this pore size distinction in applying volume fractions and transport properties. Second, the scaling may not be appropriate for catalyst layers fabricated with different materials or procedures or with porosities outside the current secondary porosity range of 0.38–0.46.

### 3.2.6 Comparison with Computational Reconstructions

We can now compare the effective diffusion coefficients and tortuosity factors reported above to those computed in prior studies from computationally reconstructed catalyst layer geometries. Our results agree well with the recent results of Lange et al. [34] when they include a local Derjaguin-type approximation of the pore length scale for Knudsen diffusion (see Eq. (13)). Our results are also similar to those of Siddique and Liu [35], but the domain in that study may be too small ( $200 \text{ nm} \times 100 \text{ nm} \times 100 \text{ nm}$ ) to accurately model a representative elementary volume. The apparent agreement likely arises from their small computed pore diameters ( $<100 \text{ nm}$ ) being offset by a low tortuosity due to the small domain size. Kim and Pitsch [21] reported tortuosity values from their computationally annealed reconstructions that qualitatively agree well with our 3D nano-CT images. Their Lattice–Boltzmann simulations predict a tortuosity value of roughly 3.5, which is notably higher than the isotropic mean tortuosity for the large sample in this work ( $\bar{\tau}_B = 2.75$ ). However, their tortuosity is still within the range of those observed for the 8 sub-samples.

Table 2 Computed transport properties for the pore phase, including volume fraction ( $\epsilon$ ), anisotropic formation factors ( $K_{f,i}$ ), anisotropy factors ( $D_{\text{eff}}^x/D_{\text{eff}}^y$ ), and Bruggeman factors (isotropic average,  $\bar{a}$ , and anisotropic,  $a_i$ ) from the fits in Figure 7.

Property	Large sample value	Sub-sample mean value $\pm$ SD	Lower bound, 95% confidence interval	Upper bound, 95% confidence interval	$R^2$
$\epsilon$	0.416	$0.417 \pm 0.016$	–	–	–
$K_{f,x}$	0.168	$0.168 \pm 0.018$	–	–	–
$K_{f,y}$	0.143	$0.147 \pm 0.014$	–	–	–
$K_{f,z}$	0.143	$0.143 \pm 0.020$	–	–	–
$D_{\text{eff}}^x/D_{\text{eff}}^y$	1.17	1.15	1.04	1.26	–
$D_{\text{eff}}^x/D_{\text{eff}}^z$	1.17	1.20	1.03	1.33	–
$\bar{a}$	–	2.15	2.09	2.21	0.57
$a_x$	–	2.04	1.96	2.12	0.71
$a_y$	–	2.20	2.10	2.12	0.48
$a_z$	–	2.22	2.13	2.32	0.77

### 3.2.7 Anisotropy and Spatial Heterogeneity

In order to evaluate the spatial heterogeneity and anisotropy, we list in Table 2 the mean values of the morphological parameters and their standard deviation in the three orthogonal directions, as well as the corresponding values for the large sample. For example, the porosity values are nearly identical between the large sample and the mean of the eight sub-samples, with only a 0.2% difference due to meshing and interpolation. However, the standard deviation across the eight sub-sample porosities is 0.016, or 4% of the porosity. In the case of the formation factors, the standard deviation is 10% of mean value, which indicates some spatial heterogeneity that can impact the uniformity of gas diffusion. It is important to note that the mean values of the formation factors agree very well with the large sample values. This agreement indicates that the smaller  $1.265^3 \mu\text{m}^3$  samples are sufficiently large to extract representative, volume averaged values and the boundaries of the model domains are not significantly intrusive.

As Figures 6 and 7 show, some anisotropy is evident in the effective diffusivities and formation factor values, with higher values in the  $x$ -direction and similar values in the  $y$ - and  $z$ -directions. Table 2 lists the ratio of the effective diffusivities for the  $x$ - and  $y$ -directions,  $D_{\text{eff}}^x/D_{\text{eff}}^y$ , and the  $x$ - and  $z$ -directions,  $D_{\text{eff}}^x/D_{\text{eff}}^z$ , for both the large sample and the mean for the eight sub-samples. In this case, the spatial heterogeneity is characterized by the 95% confidence interval for the ratios amongst the sub-samples. Both of the ratios for the large sample have a value of 1.17, indicating 17% increased transport rates in the  $x$ -direction. Similar values are found for the sub-sample mean values. However, this ratio is not systematic across all sub-samples; the lower bounds of the 95% confidence intervals are 1.04 and 1.03. Thus, the anisotropy is not significant relative to porosity and formation factor heterogeneity.

### 3.2.8 Effective Knudsen Diffusion Length Scale

As discussed in Section 0, there are a number of relevant length scales (representative pore diameters) for Knudsen diffusion in porous media as well as various interpretations of tortuosity. Zalc et al. [31] suggest that the tortuosity is a property independent of the diffusion mechanism and is equal to the value obtained for continuum diffusion with a uniform diffusion coefficient in the pore (i.e. molecular gas diffusion). In that view, the tortuosity is only a function of the structure, but is still an interpretation based on diffusive transport (though that transport is considered independent of diffusion regime). In order to realize this Knudsen regime independence for tortuosity, an appropriate Knudsen diffusion length scale must be used, such as the one derived by B.V. Derjaguin and presented later by Henrion [30], ca. Eq. (13).

We now evaluate what effective Knudsen diffusion length scale would provide the regime-independent tortuosity for our catalyst layer geometry. In this work, we use a morphological opening procedure with a spherical kernel of specified

diameter to obtain local pore diameters. The volume average (i.e. voxel average) pore diameter based on these inscribed spheres is 146 nm in the large simulation domain. Table 3 lists the formation factor, tortuosity, effective diffusivity, and volume average diffusivity in the pores when locally applying the Bosanquet formulation using these local pore diameters. In this case, the isotropic mean tortuosity is 2.75. The same table lists the formation factor and tortuosity values for molecular diffusion with a uniform diffusivity, where the isotropic mean tortuosity is 2.49. This tortuosity is lower than the Bosanquet version because of the greater diffusion resistance in smaller pores when Knudsen effects are included. Using the Bosanquet formulation, we computed what representative pore length scale,  $d_{\text{rep}}$ , yields the same tortuosity as using a uniform diffusion coefficient. In this case, the representative pore length scale is 114 nm, which is close to the inscribed sphere value of 146 nm. This value of 114 nm also compares relatively well with the length scales from the larger sample geometry used in the structural morphology analysis when based on the inscribed sphere diameter (165 nm) and the Derjaguin expression (147 nm). The mean chord length (351 nm) and the surface area based length scale (213 nm) for the larger sample volume are both significantly larger.

### 3.3 Solid Phase Tortuosity

In addition to the pore phase, we also analyzed the morphological transport properties of the solid phase. The solid phase is the combination of the carbon, Nafion, and platinum, as well as the internal micro- and meso-pores that are not resolved by the resolution of the nano-CT. The solid phase was simulated with a uniform transport coefficient without any local variations due aggregate size or composition. The solid phase data has a roughly uniform volume fraction of 0.58, with a standard deviation of 0.02 for the eight sub-samples.

Figure 8 presents the solid phase formation factor and tortuosity data for the larger sample and the eight smaller sub-samples. As before for the gas diffusion results, the mean formation factor values for the three orthogonal directions, listed in Table 4, agree well with the values from the large sample. Figure 8 also includes Bruggeman correction fits to the sub-sample formation factors. The corresponding values of  $a$  are

Table 3 Values for computing representative pore diameter,  $d_{\text{rep}}$ , based on the isotropic average formation factor and tortuosity for molecular diffusion.

Property	Large sample value
$\bar{K}_{f,B}$	0.151
$\bar{\tau}_B$	2.75
$\bar{D}_{\text{eff},B}$	$1.62 \times 10^{-6} \text{ m}^2 \text{ s}^{-1}$
$\bar{D}_B$	$10.7 \times 10^{-6} \text{ m}^2 \text{ s}^{-1}$
$\bar{d}$	146 nm
$\bar{K}_{f,m}$	0.167
$\bar{\tau}_m$	2.49
$\bar{D}_{\text{rep}}$	$9.69 \times 10^{-6} \text{ m}^2 \text{ s}^{-1}$
$d_{\text{rep}}$	114 nm

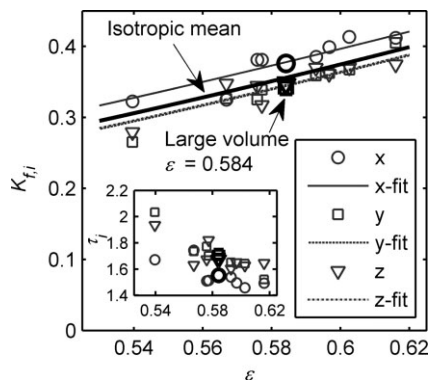


Fig. 8 Formation factor for diffusion in the solid phase. Data points are shown for the large  $2.53 \mu\text{m} \times 2.53 \mu\text{m} \times 2.53 \mu\text{m}$  sample volume (large, thick symbols) as well as the eight equally sized sub-samples versus their respective solid volume fraction for the three orthogonal directions. Bruggeman power law fits for the solid volume fraction scaling are shown for each direction and for an isotropic average (thick line). The inset shows the corresponding tortuosity factors for the large volume and the eight smaller sub-samples.

listed in Table 4. We observe improved agreement between the formation factor results and the corresponding Bruggeman corrections relative to that for the gas diffusion simulation in the pores. This is also evident in the higher  $R^2$  values for the fits (see Table 4). This difference arises because of the pore size heterogeneity of the local pore size and thus the local, Knudsen-affected diffusion coefficient in the gas diffusion simulations; transport in the solid-phase simulation has no such size dependence. As Table 4 lists, the minor effective diffusivity anisotropy computed for the pore domain is also present for the solid phase – in this case, there is a 10% increased solid phase transport rate in the  $x$ -direction.

## 4 Conclusion

Herein, we have presented an analysis of morphological and transport properties for a PEFC catalyst layer using geometry obtained by 3D nano-CT and computational simulation. The following is a list of the main conclusions we have drawn from this study.

1. Through comparisons with large sample results, we identified that a small sample volume of  $1.2 \times 1.2 \times 1.2 \mu\text{m}^3$  is sufficiently large to simulate local transport properties in the catalyst layer we imaged.
2. Although the nano-CT does not resolve the smaller mesopores or micropores, the highly restricted diffusivity in smaller pores due to amplified Knudsen effects means that they would have a small contribution to the computed overall effective diffusivities. This is supported by the good agreement between the simulated gas diffusivity and the experimentally measured value.
3. By analyzing the various proposed length scales for Knudsen diffusion, we found a chord length distribution for a PEFC catalyst layer that is statistically consistent with cylindrical pores, and that a representative pore size based on inscribed spheres agrees with the Derjaguin expression for an effective Knudsen diffusion length scale (i.e. a representative pore diameter). Alternative length-scales, e.g. those based on surface area and porosity or a mean chord length, yield significantly larger length scales.
4. When considering the volume-averaged diffusion coefficient as a reference for tortuosity estimates, the tortuosity of the pores is notably higher when including Knudsen effects in the Knudsen transition regime. Adding the series resistance of Knudsen diffusion to the molecular diffusivity increases the apparent pore-phase tortuosity from 2.49 to 2.75.
5. The isotropic Bruggeman correction factor best matching the gas diffusion simulations was 2.2. This value is significantly higher than the commonly used value of 1.5. This higher value partially arises because of increased tortuosity due to Knudsen diffusion reducing the diffusivity in smaller pores.
6. In the solid phase, the formation factor's dependence on the solid volume fraction more closely follows the Bruggeman correction scaling because the transport coefficient is uniform (does not have a local length-scale dependence) and the volume fraction is higher. The isotropic Bruggeman factor fitting the results is 1.9.
7. The nano-CT data for the PEFC catalyst layer exhibits minor diffusivity anisotropy; there is a roughly 10% higher diffusivity in one of the three orthogonal directions.

Table 4 Computed transport properties for the solid phase, including volume fraction ( $\epsilon$ ), anisotropic formation factors ( $K_{f,i}$ ), anisotropy factors  $D_{\text{eff}}^x/D_{\text{eff}}^i$ , and Bruggeman factors (isotropic average,  $\bar{a}$ , and anisotropic,  $a_i$ ).

Property	Large sample value	Sub-sample mean value $\pm$ SD	Lower bound, 95% confidence interval	Upper bound, 95% confidence interval	$R^2$
$\epsilon$	0.584	$0.584 \pm 0.024$	–	–	–
$K_{f,x}$	0.376	$0.377 \pm 0.036$	–	–	–
$K_{f,y}$	0.341	$0.344 \pm 0.041$	–	–	–
$K_{f,z}$	0.348	$0.345 \pm 0.033$	–	–	–
$D_{\text{eff}}^x/D_{\text{eff}}^y$	1.10	1.10	1.05	1.15	–
$D_{\text{eff}}^x/D_{\text{eff}}^z$	1.08	1.10	1.05	1.15	–
$\bar{a}$	–	1.92	1.88	1.97	0.69
$a_x$	–	1.81	1.75	1.87	0.81
$a_y$	–	1.99	1.92	2.05	0.87
$a_z$	–	1.98	1.91	2.04	0.80

## Acknowledgements

This material is based upon work supported by the National Science Foundation under Grant No. 1053752. The work is also supported by a STAR Fellowship Assistance Agreement FP1715401-0, awarded by the US Environmental Protection Agency (EPA) to W. Epting. The authors also wish to thank Jeff Gelb and Xradia, Inc. for their assistance in the nano-CT imaging.

## References

- [1] Z. T. Xia, Q. P. Wang, M. Eikerling, Z. S. Liu, *Can. J. Chem.-Revue Can. Chim.* **2008**, *86*, 657.
- [2] M. Lee, M. Uchida, H. Yano, D. A. Tryk, H. Uchida, M. Watanabe, *Electrochim. Acta* **2010**, *55*, 8504.
- [3] D. Papageorgopoulos, in *DOE Hydrogen Program Annual Merit Review*, Washington, DC, USA, **2010**.
- [4] S. Litster, G. McLean, *J. Power Sources* **2004**, *130*, 61.
- [5] M. Uchida, Y. Aoyama, N. Eda, A. Ohta, *J. Electrochem. Soc.* **1995**, *142*, 4143.
- [6] C. Johnston, in *DOE Hydrogen Program Annual Merit Review*, Arlington, VA, USA, **2009**.
- [7] K. Malek, M. Eikerling, Q. P. Wang, T. C. Navessin, Z. S. Liu, *J. Phys. Chem. C* **2007**, *111*, 13627.
- [8] T. A. Greszler, D. Caulk, P. Sinha, *J. Electrochem. Soc.* **2012**, *159*, F831.
- [9] W. K. Epting, S. Litster, *Int. J. Hydrogen Energy* **2012**, *37*, 8605.
- [10] K. Kudo, T. Suzuki, Y. Morimoto, *ECS Trans.* **2010**, *33*, 1495.
- [11] W. Sun, B. A. Peppley, K. Karan, *Electrochim. Acta* **2005**, *50*, 3359.
- [12] C. Ziegler, S. Thiele, R. Zengerle, *J. Power Sources* **2011**, *196*, 2094.
- [13] S. Zils, M. Timpel, T. Arlt, A. Wolz, I. Manke, C. Roth, *Fuel Cells* **2010**, *10*, 966.
- [14] E. A. Wargo, A. C. Hanna, A. Cecen, S. R. Kalidindi, E. C. Kumbur, *J. Power Sources* **2012**, *197*, 168.
- [15] N. S. K. Gunda, H.-W. Choi, A. Berson, B. Kenney, K. Karan, J. G. Pharoah, S. K. Mitra, *J. Power Sources* **2011**, *196*, 3592.
- [16] J. R. Izzo, Jr., A. S. Joshi, K. N. Grew, W. K. S. Chiu, A. Tkachuk, S. H. Wang, W. Yun, *J. Electrochem. Soc.* **2008**, *155*, B504.
- [17] P. R. Shearing, J. Gelb, N. P. Brandon, *J. Eur. Ceram. Soc.* **2010**, *30*, 1809.
- [18] P. R. Shearing, J. Golbert, R. J. Chater, N. P. Brandon, *Chem. Eng. Sci.* **2009**, *64*, 3928.
- [19] J. R. Wilson, A. T. Duong, M. Gameiro, H.-Y. Chen, K. Thornton, D. R. Mumm, S. A. Barnett, *Electrochem. Commun.* **2009**, *11*, 1052.
- [20] W. K. Epting, J. Gelb, S. Litster, *Adv. Funct. Mater.* **2012**, *22*, 555.
- [21] S. H. Kim, H. Pitsch, *J. Electrochem. Soc.* **2009**, *156*, B673.
- [22] K. J. Lange, P. C. Sui, N. Djilali, *J. Electrochem. Soc.* **2010**, *157*, B1434.
- [23] P. P. Mukherjee, C. Y. Wang, *J. Electrochem. Soc.* **2006**, *153*, A840.
- [24] A. Tkachuk, F. Duewer, H. T. Cui, M. Feser, S. Wang, W. B. Yun, *Z. Kristall.* **2007**, *222*, 650.
- [25] A. Cecen, E. A. Wargo, A. C. Hanna, D. M. Turner, S. R. Kalidindi, E. C. Kumbur, *J. Electrochem. Soc.* **2012**, *159*, B299.
- [26] *CRC Handbook*, 92nd (Ed. D. R. Linde), CRC Press, Boca Raton, FL, USA, **2012**.
- [27] N. Epstein, *Chem. Eng. Sci.* **1989**, *44*, 777.
- [28] R. E. De La Rue, C. W. Tobias, *J. Electrochem. Soc.* **1959**, *106*, 827.
- [29] T. Berning, D. M. Lu, N. Djilali, *J. Power Sources* **2002**, *106*, 284.
- [30] P. N. Henrion, *Powder Technol.* **1977**, *16*, 159.
- [31] J. M. Zalc, S. C. Reyes, E. Iglesia, *Chem. Eng. Sci.* **2004**, *59*, 2947.
- [32] A. Berson, H.-W. Choi, J. G. Pharoah, *Phys. Rev. E* **2011**, *83*.
- [33] Z. Yu, R. N. Carter, *J. Power Sources* **2010**, *195*, 1079.
- [34] K. J. Lange, P.-C. Sui, N. Djilali, *J. Power Sources* **2012**, *208*, 354.
- [35] N. A. Siddique, F. Q. Liu, *Electrochim. Acta* **2010**, *55*, 5357.